

ARTICLE OPEN



Porous perovskite films integrated with Au–Pt nanowire-based electrodes for highly flexible large-area photodetectors

Rohit Saraf¹, Hua Fan¹ and Vivek Maheshwari¹

Flexible, large-area, and stable perovskite photodetectors have drawn increasing widespread research attention for next-generation wearable and portable optoelectronic devices. However, high mechanical durability coupled with large device area and enhanced environmental stability has not been demonstrated yet to attain practical viability. Herein, a highly bendable, stable, and large-area (3 cm²) flexible polystyrene incorporated perovskite photodetector is presented. Due to the formation of a porous polystyrene-perovskite composite film in a single step it allows unprecedented mechanical stability, maintaining 85% of its original photocurrent value after 10,000 bending cycles at a bending angle of 120°. Equally crucial, the solution-processed self-assembled Pt–Au nanochains were developed to provide a simple and fast method of patterning the conductive and flexible electrodes onto the filter substrate. The optimized polystyrene-perovskite photodetector exhibits a high responsivity up to 2.73 A W⁻¹, a maximum specific detectivity of 6.2 × 10¹³ Jones, and a superior switching ratio of 1.0 × 10⁴. In addition, the polystyrene-perovskite photodetector yields excellent stability under the combined stresses of moisture, ambient air, and room light, and retains 92% of its original performance for over 30 days. All these results demonstrate that this work provides a facile and cost-effective approach that paves the way to develop high-performance, stable, and highly flexible optoelectronic devices.

npj Flexible Electronics (2020)4:30; <https://doi.org/10.1038/s41528-020-00094-5>

INTRODUCTION

Large-area, cost-effective, and flexible photodetectors are required in multiple applications such as next-generation wearable optoelectronics, robotics, bio-imaging, illumination monitoring systems, and remote sensing^{1–5}. Organometal halide perovskites, specifically CH₃NH₃PbI₃ (or MAPbI₃) has emerged as outstanding light-harvesting material in the optoelectronic field due to its long charge carrier diffusion length, low exciton binding energy, broadband absorption, and direct bandgap^{6–9}. The added advantage of their solution based low-temperature fabrication process makes them suitable for application in flexible electronics and photonic devices^{10,11}. Flexibility is primarily defined by the ability to bend these devices to achieve a low form factor or easy integration with a curved surface for mounting on non-traditional spaces. The common strategy in perovskite photodetectors (and others) for reducing the maximum strain on bending has been based on two common themes, 1. By making nano/micro-wire arrays to limit the dimensions of the material^{12–14}, or 2. Using thin perovskite films to reduce the thickness^{4,15,16}. Combined with the inherent challenge of stability in perovskites, either of these strategies has limited success and as a result, most of the previous reports on flexible perovskite photodetectors, either conducted only a few hundred bending cycles test at large bending radii or suffer from poor environmental stability^{4,12,15,16}. Progress has been made recently in improving stability by encapsulation of the perovskite layer, along with achieving ultra-fast response time in photodetectors^{17,18}. It is also worth noting that most of the reported performances for flexible perovskite photodetectors are on the very small area < 0.4 cm² and very few reports exist on the large area (>1 cm²) devices^{4,19,20}. Therefore, there is a need to perform further studies and improve on the repeatable bending durability, while stabilizing the device performance. Further to ensure cost-effectiveness facile manufacturing processes resulting

in large-area photodetectors, without significantly affecting the performance characteristics of the material are required.

Here, we demonstrate a highly bendable (10,000 cycles), stable, and large-area (3 cm²) flexible polystyrene (PS) incorporated MAPbI₃ photodetectors. The high bendability is achieved by having a thin porous film of perovskite made by spin casting. This combines the effect of lowering the bending strain due to, the small thickness of the film and a lower modulus from the porous structure. The specific interaction between PbI₂ and MAI in the perovskite precursor solution and PS chains results in the formation of a cross-linked polymer-perovskite network, which assists in enhancing the performance and improving the stability of the PS-MAPbI₃ photodetectors. In this work, we used microporous polyamide filters as the flexible substrate for fabricating large-area photodetectors, owing to their excellent bendability, durability, good recyclability, and low-cost. The other significant challenge that needs to be addressed for making flexible devices is the requirement of equally durable and flexible high-performance electrodes²¹. The mechanical and electrical properties of electrodes fabricated on soft and bendable substrates degrade gradually due to fatigue damage during repeated deformations. To address this key issue, we synthesized self-assembled platinum–gold (Pt–Au) nanoparticle chains and deposited them on the polyamide filters by simple vacuum filtration to fabricate the patterned Pt–Au electrodes. This approach shows significant advantages in terms of conductivity, ease of fabrication, cost-effectiveness, and compatibility with the soft and flexible substrates used for the devices. In addition, the solution-processed self-assembled Pt–Au nanoparticles chains patterned as electrodes are highly bendable and provide a simple and fast method for fabricating flexible metal electrodes.

The optimum 1 wt % PS-MAPbI₃ device exhibits a low dark current of 1.1 nA at 2 V, a high responsivity of 2.73 A W⁻¹, a large detectivity of 6.2 × 10¹³ Jones, and a superior switching ratio of

¹Department of Chemistry, Waterloo Institute for Nanotechnology, University of Waterloo, Waterloo, ON N2L 3G1, Canada. ✉email: vmaheshw@uwaterloo.ca

1.0×10^4 as compared to plain MAPbI₃ device. Furthermore, the 1 wt % PS-MAPbI₃ flexible photodetector shows outstanding bending stability and retains a photocurrent of 85% of its initial value after 10,000 bending cycles at a bending angle of 120°. This also illustrates the robustness of the nanoparticle electrodes for bending. Under the same bending conditions, a substantial decrease in photocurrent to 50% was observed for plain MAPbI₃ device. Finally, the 1 wt % PS-MAPbI₃ flexible photodetector shows excellent stability and retains 92% of its original value even after 30 days (720 h) of continuous exposure of moisture, ambient air, and under room light, which was far better than that of the plain MAPbI₃ photodetector whose performance significantly deteriorates to almost zero after 8 days (192 h). This facile fabrication process of large-area flexible photodetectors with superior bending robustness coupled with improved environmental stability and reduced cost will pave the way for next-generation wearable and smart optoelectronics.

RESULTS AND DISCUSSION

Fabrication and opto-electronic performance

A schematic representation of the fabrication process of flexible PS-MAPbI₃ photodetector is shown in Fig. 1a, b. First, the highly conductive Pt–Au electrodes were deposited on the flexible polyamide filter membrane (see *I–V* curves of Pt–Au electrodes in Supplementary Fig. 1) by solution filtration of micron size long-chain networks of Au nanoparticles self-assembled in a solution using Pt⁴⁺ ions and then reduced to form continuous Pt–Au nano-networks. The TEM and high-resolution TEM (HRTEM) images of Pt–Au nanochains are presented in Supplementary Fig. 2. The TEM image illustrates the typical Pt–Au nanoparticles (~microns in size, with local nanowire width of ~5–10 nm) chain structure. The pore size of the polyamide filter is around 1–2 μm as observed in the field emission scanning electron microscopy (FESEM) image (Fig. 1a). Then, the PS containing MAPbI₃ (or plain MAPbI₃) precursor solution was spin-coated and annealed on 2.0 × 1.5 cm² area Pt–Au-patterned polyamide substrate (shown in Fig. 1b). The cross-sectional FESEM images shown in Supplementary Fig. 3 illustrate that the thickness of the plain MAPbI₃ and 1 wt % PS-MAPbI₃ films are around 1.010 and 1.038 μm, respectively. The porous structure of the polyamide filter would lead to the formation of a porous perovskite structure on the filter during the spin-coating process. A FESEM image of the resulting porous PS-MAPbI₃ films is shown in Fig. 1b. A similar approach was used to fabricate the porous plain MAPbI₃ (without PS) films on the polyamide filter. A photograph of the Pt–Au electrodes on the flexible polyamide filter is displayed in Fig. 1c. Figure 1d and e shows the photograph of the resulting PS-MAPbI₃ device and its flexibility. The details of the fabrication process are in the experimental section. The Lewis-acid characteristic of PbI₂ leads to the interaction between PS and MAPbI₃ precursors and cross-linking of the polymer chains. While the cation-π electron interactions are the basis of coupling between the MAI and PS chains. We have confirmed and reported these interactions in our previous work^{22,23}. The impact of PS incorporation into the perovskite was evaluated by X-ray diffraction (XRD), and UV–Vis absorption spectroscopy. The diffraction patterns (Fig. 1f) showed no obvious changes with and without PS, and all the samples exhibit the same tetragonal perovskite crystal structure with the dominant (110) lattice plane. As displayed in Fig. 1g, the UV–Vis absorption spectra show a broad absorption in the range of 300–780 nm, indicating high light-harvesting capabilities over the ultraviolet to the visible spectrum. There is a small difference in the absorption value that can be due to the slight variation (±50 nanometers, Supplementary Fig. 3) in the thickness of the perovskite films, which revealed that the absorption properties of MAPbI₃ films with and without PS are preserved.

The photocurrent generation from the flexible PS-MAPbI₃ photodetector is schematically depicted in Fig. 2a. Our photodetector is based on the photoelectric effect in which the applied voltage results in an electric field that leads to the effective separation of electrons and holes generated on light illumination. Due to the close matching of the work function of Pt–Au (5.2 eV) with the highest occupied molecular orbital (HOMO) of PS-MAPbI₃ perovskite (5.4 eV), the collection of holes are favorable by the negative Pt–Au electrode in the symmetric Pt–Au/PS-MAPbI₃ (or MAPbI₃)/Pt–Au device. Whereas, the electrons are not easily collected (or get trapped) due to the large energy level difference between the Lowest Unoccupied Molecular Orbital (LUMO) of PS-MAPbI₃ (3.9 eV) and work function of Pt–Au (5.2 eV). Figure 2b presents the photoresponse from both plain MAPbI₃ and PS-MAPbI₃ devices (with varying concentrations of PS) at 2 V and under the illumination of 1.0 sun. The plain MAPbI₃ device showed a photocurrent of 2.8 μA, which enhanced with the incorporation of PS. Specifically, the photocurrent for 0.5 wt % PS-MAPbI₃ device is 4.8 μA, and it increased substantially to 11.2 μA for 1 wt % PS-MAPbI₃ device. We attribute this to the fewer defects and suppressed charge carrier recombination by the cross-linking of PS within MAPbI₃²². Further, the addition of PS to 3 and 7 wt % caused a drop in photocurrent to 6.9 and 1.1 μA, respectively. The corresponding light switching on/off ratios is illustrated in Supplementary Fig. 4, and it also follows a similar trend. It is worth noting that the light switching ratio for 1 wt % PS-MAPbI₃ device (1.0×10^4) is 1 order of magnitude higher than that of plain MAPbI₃ device (1.0×10^3). The comparison reveals that among all the above PS concentrations, 1 wt % PS device gives the best performance due to the highest carrier lifetime and mobility, and simultaneously lowest, charge recombination effects, the density of defect traps, and ion migration, and therefore it was characterized in detail²². The dark currents and photocurrents were measured to quantitatively compare the performance of photodetectors made with both plain MAPbI₃ and 1 wt % PS-MAPbI₃. For both the photodetectors, with increasing voltage the dark currents and photocurrents increase (Fig. 2c) due to greater strength of the electric fields, as it leads to more effective charge separation and collection. The 1 wt % PS-MAPbI₃ device exhibits a better performance with ~3 times lower dark current and ~4 times higher photocurrent than the plain MAPbI₃ devices. This can be attributed to the presence of PS (insulating material), reduced ion-migration effects, and lower carrier recombination in PS-MAPbI₃ photodetectors²². The photoresponse curves of the optimized 1 wt % PS-MAPbI₃ photodetector as a function of different wavelengths (410–710 nm) at a low bias of 2 V are presented in Fig. 2d. The photocurrent of the device was measured to be 26, 22, 28, 40, 45, and 22 nA under 410, 475, 520, 585, 650, and 710 nm light irradiation, respectively. The device shows a consistent and stable response over the cycles under monochromatic light. To quantitatively evaluate the output performance of plain MAPbI₃ and 1 wt % PS-MAPbI₃ photodetectors, their spectral responsivity (Fig. 2e), detectivity (Fig. 2e), and external quantum efficiency (Supplementary Fig. 5) were measured. The responsivity (*R*) and detectivity (*D*^{*}) are defined as^{24,25}

$$R = \frac{I_{ph} - I_d}{P_{in}} \quad (1)$$

$$D^* = \frac{R}{\sqrt{2qI_d/A}} \quad (2)$$

where *I*_{ph} is the photocurrent, *I*_d is the dark current, *P*_{in} is the incident light power, *q* is the electron charge, and *A* is the effective area of the photodetector. The responsivity and detectivity of the 1 wt % PS-MAPbI₃ photodetector (Fig. 2e) in the spectral range from 400 to 750 nm are 5 and 7.5 times higher than the plain MAPbI₃ photodetector, respectively. We observe that the 1 wt % PS-MAPbI₃ device attains a maximum responsivity of 0.25 A W⁻¹

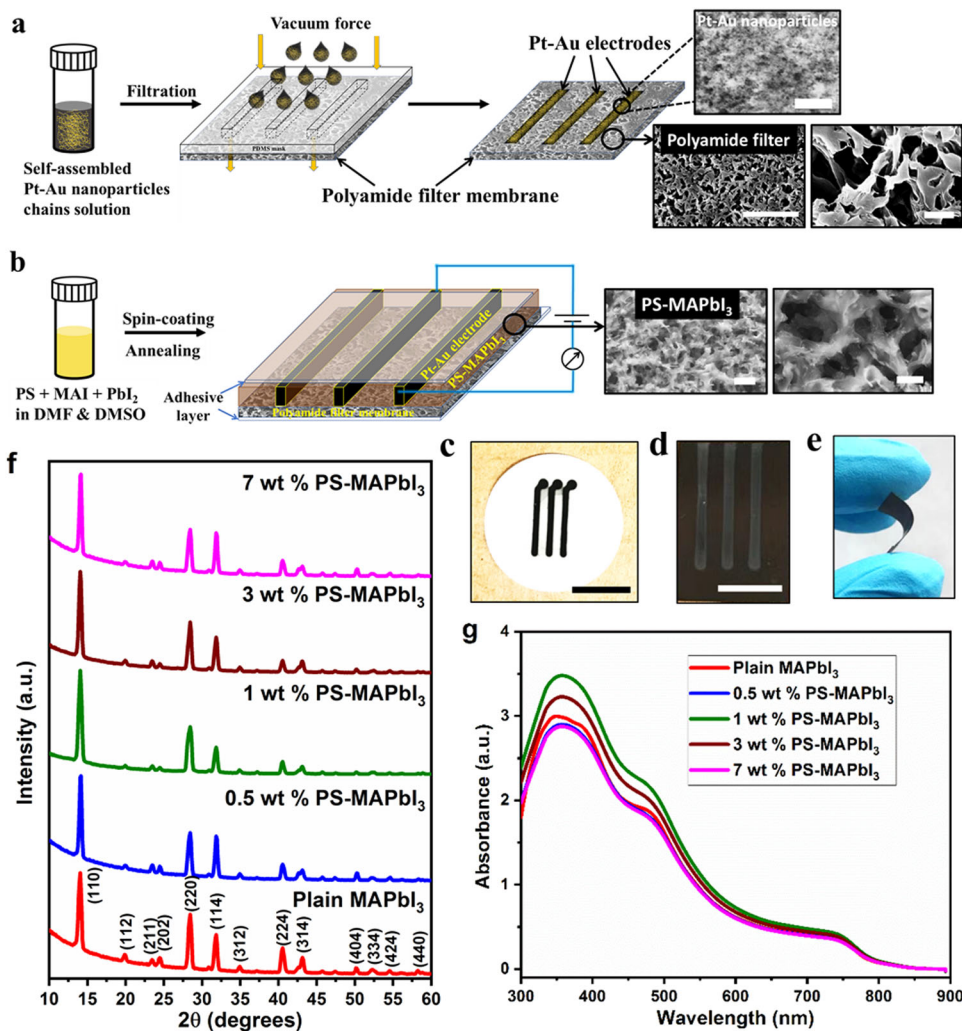


Fig. 1 Fabrication process and characterization of flexible PS-MAPbI₃ photodetectors. **a** Deposition of Pt–Au electrodes using self-assembled Pt–Au nanoparticles chains solution on polyamide filter membrane, with the FESEM image (on the right) shows the Pt–Au nanoparticles (~10 nm) chain structure with the 200 nm scale bar and the 1–2 μm pore size of the polyamide filter with the scale bars represent 10 μm (left image) and 1 μm (right image). **b** Deposition of PS-MAPbI₃ film on Pt–Au-patterned polyamide filter. The lower resolution (left image with 2 μm scale bar) and higher resolution (right image with 1 μm scale bar) FESEM images show the porous PS-MAPbI₃ film. Photograph of the **c** Pt–Au electrodes on the flexible substrate with the 1 cm scale bar, **d** final PS-MAPbI₃ device with a 4 mm scale bar, and **e** bending (or flexibility) of the device. **f** XRD patterns and **g** UV–Vis absorption spectra of plain MAPbI₃, 0.5, 1, 3, and 7 wt % PS-MAPbI₃ films.

and detectivity of 5.7×10^{12} Jones under illumination by monochromatic light with a wavelength of 650 nm. The corresponding external quantum efficiency (EQE) of 1 wt % PS-MAPbI₃ device is greater than that of the plain MAPbI₃ device as shown in Supplementary Fig. 5. The photoresponse of 1 wt % PS-MAPbI₃ device irradiated by 650 nm light of different intensities (0.001 – 10 mW cm^{-2}) is shown in Fig. 2f. The photocurrent increases with the light intensity, which can be ascribed to the increased number of photogenerated charge carriers in response to the higher photon flux²⁶. It should be noted that the photocurrent at very low intensity (0.001 mW cm^{-2} or $1 \mu\text{W cm}^{-2}$) of 650 nm light is 45 nA, which is more than 1 order of magnitude higher than that under dark conditions (1.1 nA). The corresponding responsivity and detectivity are shown in Supplementary Fig. 6. The response time of the 1 wt % PS-MAPbI₃ photodetector was also determined and found to be <5 ms, which is the detection limit of our setup (Supplementary Fig. 7). The responsivity and detectivity of plain MAPbI₃ and 1 wt % PS-MAPbI₃ photodetectors using 2 V at different light intensities by attenuating 1.0 sun illumination (from solar simulator) using neutral density filters is presented in Fig. 2g. The maximum value

of R and D^* for 1 wt % PS-MAPbI₃ device is 2.73 A W^{-1} and 6.2×10^{13} Jones at illumination intensity of 0.001 mW cm^{-2} , which is comparable and even higher than the previous reports on the flexible photodetectors (Table 1)^{3,12,13,20,27–38}. In contrast, the plain MAPbI₃ device achieves only R (0.61 A W^{-1}) and D^* (0.86×10^{13} Jones), which implies that the incorporation of 1 wt % PS in MAPbI₃ greatly improved the photodetector performance. The higher R and D^* observed under illumination from the solar simulator (a broad-spectrum source) compared to illumination at 650 nm is attributed to the broad absorption spectrum of MAPbI₃ which leads to greater absorption of photons of higher energies.

Flexibility and operational stability

As mechanical stability is the major concern for the practical feasibility of flexible photodetectors for wearable electronics, we studied the bending durability of both plain MAPbI₃ and 1 wt % PS-MAPbI₃ photodetectors. Figure 3a shows the schematic representation of the bending of the flexible PS-MAPbI₃ photodetector. The device was bent at varied angles as shown in the inset of Fig. 3b, and the photocurrent was measured during the

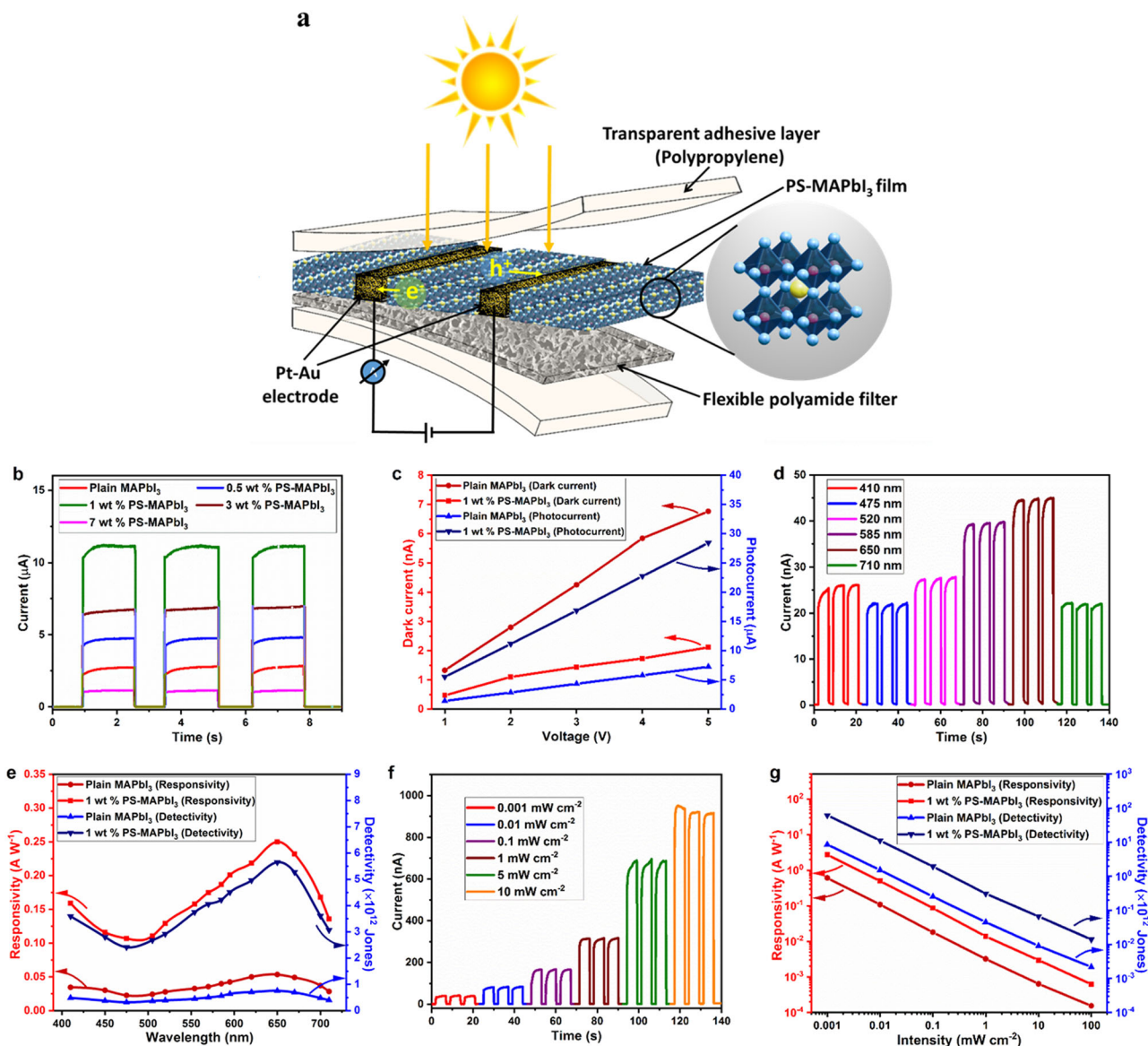


Fig. 2 Device configuration, operation mechanism, and its performance. **a** Schematic diagram showing the current generation by light irradiation from the flexible PS-MAPbI₃ photodetector. **b** Photoresponse cycles of the plain MAPbI₃ and different concentrations of PS-MAPbI₃ devices at 2 V under 1.0 sun illumination. **c** Dark and photocurrent of the devices at different voltages under one sun illumination. **d** Photoresponse of the 1 wt % PS-MAPbI₃ device under the illumination of different wavelengths at 2 V. **e** Responsivity and detectivity of the devices at 2 V and under fourteen different wavelengths ranging from 410 to 710 nm. **f** Photoresponse curves of the 1 wt % PS-MAPbI₃ device at 2 V and under 650 nm light wavelength at various power intensities. **g** Spectral responsivity and detectivity of the devices as a function of different light intensities at 2 V under white light. Typical measurements were conducted on multiple devices (at least 4) and yield an error range of 3–5% for all the samples.

bending to ensure the performance reliability of the flexible device. The photocurrent of both flexible devices remains unchanged with the bending angle varying from 0° to 120° (Fig. 3b). Even at the maximum bending angle of 180°, there is a slight decrease in photocurrent which can be due to the reduction of the light-receiving area at the bending state. The photocurrent retained to its original value as the device brings back to zero bending angles. Further, we measured the photocurrent of both devices after bending for 10,000 cycles at a fixed bending angle of 120° and a bending radius of 1.5 mm. For clarity, all the photocurrents were normalized to their respective initial values. As can be seen in Fig. 3c, the photocurrent of the 1 wt % PS-MAPbI₃ device maintained 100, 91, and 85% of its initial value after 1000, 5000, and 10000 bending cycles, whereas under the same bending conditions for plain MAPbI₃ devices the

photocurrent dropped to 90, 68, and 50% of its initial value. The photodetectors are also evaluated for their long-term stability in operation. The plain MAPbI₃ and 1 wt % PS-MAPbI₃ devices with and without an adhesive layer were tested upon exposure to the ambient environment (in the air at a relative humidity of 35–40% under room light). Figure 3d shows the 1 wt % PS-MAPbI₃ devices maintain 92% of its initial photocurrent value after 720 h (30 days). In contrast, the plain MAPbI₃ devices completely degrade in just 192 h (8 days) with more than 60% loss within 3 days. Similarly, we also achieved a better stability for the 1 wt % PS-MAPbI₃ device without an adhesive layer in the ambient environment as compared to the plain MAPbI₃ device (Supplementary Fig. 8). The improved stability of 1 wt % PS-MAPbI₃ devices can be attributed to the combined effects of the presence of PS (hydrophobic in nature) which leads to passivation of defects,

Table 1. Performance comparison with some previously reported flexible perovskite-based photodetectors.

Flexible substrate	Device structure	Bias (V)	Response range	R ($A W^{-1}$)	D^* ($\times 10^{12}$ Jones)	Bending cycles (bending radius or angle)	Ref.
Polyamide filter	Pt–Au/PS-MAPbI ₃ /Pt–Au	2	White light 650 nm	2.73 0.25	62 5.7	10,000 (120°)	This work
PEN	ITO/NIO SnO ₂ / perovskite/Spiro-OMeTAD/Ag	0	720 nm	0.473	13.5	500 ($R = 4$ mm)	3
PEN	Au/P(VDF-TrFE)/MAPbI ₃ nanowires/Au	0	650 nm	0.012	7.3	200 (180°)	12
Kapton	Au/MAPbI _{3-x} (SCN) _x /PMMA/Au	10	White light	0.62	7.3	12000 ($R = 1$ cm)	13
PEN	Ag/Spiro-OMeTAD/MAPbI ₃ /In ₂ S ₃ /ITO	0	720 nm	0.451	0.11	500 ($R = 2.5$ mm)	20
Polyimide	Au/MAPbI ₃ /Au	0	300 nm	0.002	0.176	($R = 3.7$ mm)	27
PET	Au/CsPbBr ₃ /Au	2	254 nm 365 nm 540 nm	0.00024 0.00055 0.00002	0.019 0.044 0.0016	220 ($R = 19.94$ mm)	28
PET	Ni/Au/MAPbI _{3-x} Cl _x /Ni/Au	5	650 nm	2.17	0.94	500 (150°)	29
PET	ITO/CsPbBr ₃ /ITO	10	517 nm	0.64	–	10,000 (80°)	30
PET	Au/PbPc/MAPbI _{3-x} Cl _x /Au	50	655 nm	0.152	0.85	1000 ($R = 6.5$ mm)	31
PEN	Au/MAPbI ₃ /RhB/Au	5	550 nm	0.0436	–	1000 ($R = 9$ mm)	32
Common paper	Ti ₃ C ₂ T _x /CsPbBr ₃ nanosheets/Ti ₃ C ₂ T _x	10	450 nm	0.0449	0.00064	1500 (160°)	33
PEN	Au/P(VDF-TrFE) /MAPbI ₃ /Au	0	650 nm	0.02	14	200 (180°)	34
PET	Au/CsPbBr ₃ /ZnO/Au	210	515 nm	<1 4.25	–	10,000 ($R = 2.5$ mm)	35
PET	Ag/CsPbBr ₃ nanosheets/CNTs/Ag	10	442 nm	31.1	–	10,000	36
PET	MAPbI ₃ /C8BTBT bulk heterojunction	3	532 nm	8.1	2.17	10,000 ($R = 7.5$ mm)	37
PET	Au/FA _(1-x) Cs _x Pb[Br _y I _(1-y)] ₃ /Au	1	450 nm	1.1	28	10000 ($R = 3$ mm)	38

and reduced ion-migration effects^{22,39}. Further to ensure the reliability of the photoresponse measurement, the photoresponse of the plain MAPbI₃ and 1 wt % PS-MAPbI₃ devices were recorded as a function of time at 2 V under 650 nm light irradiation (0.1 mW cm⁻² intensity), as presented in Fig. 3e. Both the devices exhibited very stable performances. Measured for 60 min, the photocurrent of the plain MAPbI₃ device was measured to be at 37 nA, whereas the 1 wt % PS-MAPbI₃ device exhibited a photocurrent of 169 nA. These results demonstrate that our 1 wt % PS-MAPbI₃ photodetector has excellent mechanical flexibility and durability as well as outstanding environmental stability. The mechanical stability is also attributed to the porous and chain-like structure of the Pt–Au electrode (Supplementary Fig. 2) which can endure repeated bending without failure. It also shows that the Pt–Au electrode remains chemically stable for days and under device operating conditions, without any degradation with the perovskite layer. Ag nanowires in comparison can undergo redox reactions with the perovskite layer with relative ease impacting stability^{40–42}. Ag nanowires also have the challenge of mechanical and thermal stability and junction resistance⁴³. Further the Pt–Au electrodes are made using a room temperature based self-assembly process for synthesis and simple vacuum filtration for control of the deposition process. The conductivity/cost ratio of the Pt–Au electrodes is ~63,000 Sm⁻¹/US\$, while for Ag nanowire-based electrodes this can range from 8000–123,000 Sm⁻¹/US \$, making them comparable in cost. It is also higher than pure Au electrodes (1023 Sm⁻¹/US \$)^{21,44}.

In summary, we have demonstrated the feasibility of using PS-incorporated MAPbI₃ networks to develop a porous film on a flexible filter membrane for fabricating large-area ultra-flexible photodetector. Low-cost flexible Pt–Au electrodes were patterned

by using the facile solution-processed self-assembled nanochains. The optimum 1 wt % PS-MAPbI₃ device showed extremely high bending stabilities, maintaining a photocurrent of 85% of their original values after 10,000 bending cycles under a large bending angle ($\theta = 120^\circ$). The responsivity and detectivity of 1 wt % PS-MAPbI₃ flexible photodetector reached 2.73 A W⁻¹ and 6.2×10^{13} Jones, respectively. This is among the best-reported performance with high mechanical durability when compared to other flexible perovskite photodetectors. Moreover, the PS incorporation in MAPbI₃ showed long-term device stability for more than 30 days in the ambient environment. The presented low-cost, ultra-flexible, highly stable, and large-area photodetectors will lay a strong foundation for developing next-generation wearable and portable optoelectronic devices.

METHODS

Preparation of Pt–Au nanoparticles chains

Hundred and thirty microliters of 4.5 mg mL⁻¹ platinum (IV) tetrachloride (PtCl₄, Sigma Aldrich) were mixed with 1 mL citrate capped gold nanoparticles (~10 nm) solution, purchased from BBI Solutions OEM Limited, and then left on the shaker until the solution color changed to dark blue due to the self-assembly of Au nanoparticles. Seventy-five microliters of 4 mg mL⁻¹ sodium borohydride (NaBH₄) was then added to reduce the Pt⁴⁺ ions, the color of the solution changes from initial dark blue to black due to the formation of Pt metal.

Preparation of MAI precursor

Methylammonium iodide (MAI) was synthesized by dropwise addition of 30 mL of hydroiodic acid (Sigma-Aldrich, 57 wt. % in water) to 27.8 mL of methylamine (Sigma-Aldrich, 33 wt. % in absolute ethanol) under constant

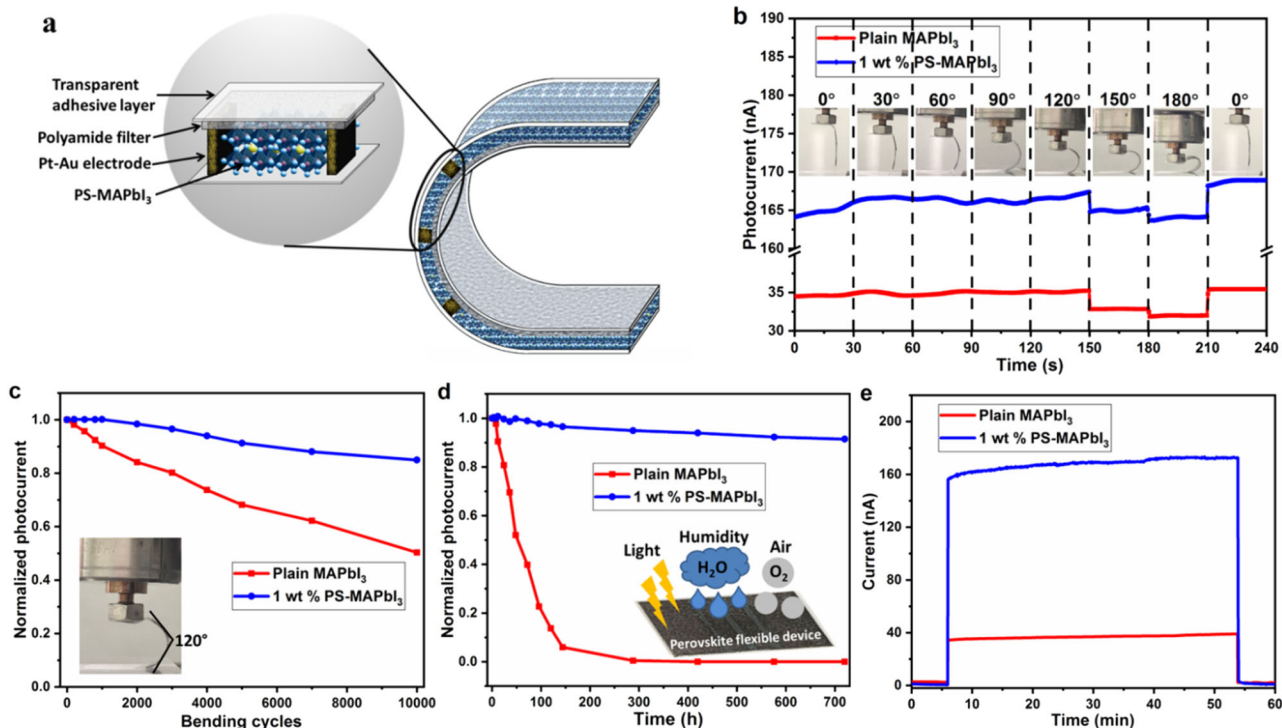


Fig. 3 Bending and stability test of the flexible photodetectors. **a** Schematic showing the bending of the flexible PS-MAPbI₃ photodetector. **b** Photocurrent response of the plain MAPbI₃ and 1 wt % PS-MAPbI₃ devices under 650 nm light illumination at 0.1 mW cm⁻² intensity during the bending process. The inset shows the corresponding optical images of the device under different bending angles. **c** Normalized photocurrent of the flexible devices after different bending cycles at a bending angle of 120° showing the mechanical stability and durability of 1 wt % PS-MAPbI₃ device even after 10000 bending cycles. **d** Normalized photocurrent of the devices with an adhesive layer during aging continuously in ambient air, 35–40% relative humidity, and under room light for 720 h (30 days). **e** Operational stability of the devices at a constant bias of 2 V under 650 nm light irradiation of 0.1 mW cm⁻² intensity. Typical measurements were conducted on multiple devices (at least 4) and yield an error range of 3–5% for all the samples.

stirring at 0 °C for 2 h. A dark yellow precipitate was recovered using a rotary evaporator at 60 °C for 1 h. The precipitate was then washed and recrystallized with a copious amount of diethyl ether and ethanol, respectively, until it turned white. The resultant white precipitate was dried in vacuum overnight to obtain the final pure MAI.

Preparation of plain MAPbI₃ and PS-MAPbI₃ solutions

The 1.35 M of plain MAPbI₃ solution (without PS) was prepared by mixing 230.5 mg of lead iodide (PbI₂), 79.5 mg of MAI in 53.3 μL of dimethyl sulfoxide (DMSO) and 317.5 μL of dimethylformamide (DMF) for 1 h. To prepare the 0.5, 1, 3, and 7 wt % PS-MAPbI₃ solutions, the required amount of PS (PS, Alpha Chemistry, *M_w* = 45,000) was dissolved in DMSO and DMF and stirred constantly for 30 min. Then, MAI and PbI₂ (1/1 by molar) were added to the above PS solution under constant stirring for 1 h (time for crosslinking) at room temperature. The entire process was carried out in ambient conditions.

Fabrication of flexible photodetectors

The polyamide filter membranes with a 25 mm diameter were purchased from GE Healthcare. The self-assembled Pt–Au nanochains solution was used to deposit the flexible and highly conductive Pt–Au electrodes on the polyamide membrane through the vacuum-filtration process. The PDMS mask was used during the vacuum filtration to obtain a certain Pt–Au patterned electrode. The distance between the Pt–Au electrodes was 1.6 mm, the thickness of Pt–Au electrodes was around 550 nm and was kept constant for all samples. 90 μL of plain MAPbI₃ or PS-MAPbI₃ solution was then spin-coated on the polyamide filter membrane patterned with Pt–Au electrodes at 4000 rpm for 30 s. After 8 s of rotation, 200 μL of diethyl ether was dropped onto the center of the flexible polyamide substrate. The obtained films were then heated at 100 °C for 10 min to form the perovskite phase. The thickness of the MAPbI₃ perovskite films with and without PS was around 1 μm (±50 nm). Finally, transparent self-adhesive tape was used to cover the perovskite films. The device

configuration was Pt–Au/PS-MAPbI₃ (or MAPbI₃)/Pt–Au on the polyamide filter.

Characterization and measurement

The surface morphology of the self-assembled Pt–Au nanoparticles, polyamide filter, and perovskite films was observed by FESEM (FESEM, Zeiss Ultraplus). Transmission electron microscopy (TEM) images were obtained with a LEO 912AB transmission electron microscope. The phase of the perovskite samples was characterized by X-ray diffraction (XRD) using a PANalytical Empyrean diffractometer with Cu-Kα radiation ($\lambda = 1.54 \text{ \AA}$). The optical absorption spectra were recorded using a UV–Visible spectrophotometer (Perkin Elmer Lambda 750). The photoelectrical measurements of the device under different light wavelengths and intensities, including *I*–*V*, photocurrent, dark current, spectra responsivity, detectivity, and EQE were recorded by a Keysight 3458 A Digital multimeter combined with 6614 C 50 Watt system power supply from Agilent Technologies in ambient condition. All the measurements on Pt–Au/PS-MAPbI₃ (or MAPbI₃)/Pt–Au devices were conducted on the probing station by using a two-probe method. The voltage was applied on the plain MAPbI₃ or PS-MAPbI₃ porous films by connecting one probe to the first Pt–Au electrode on the filter and another probe connected to the second Pt–Au electrode. Simulated AM 1.5 G irradiation (100 mW cm⁻²) with a xenon-lamp based solar simulator (Newport Oriel Instrument 67005, 150 W Solar Simulator) was used as the illumination source. The Newport optical filters were used to produce incident light at various intensities. The light intensity was calibrated by an NREL calibrated KG5 silicon reference cell to minimize spectral mismatch. All measurements were conducted at room temperature and in ambient air. The active area of the devices was 1.2 cm². For the bending test, an MFA motorized miniature linear stage was used to bend the flexible device at a particular angle and to perform 10,000 bending cycles at a constant speed. The long-term stability test of the devices was tested by directly exposing the devices in ambient air with 35–40% relative humidity and under room light. The humidity was

measured by a portable RH sensor and was controlled by adjusting the flow rate of the carrier gas (dry N₂).

DATA AVAILABILITY

All relevant data in this study are available from the corresponding author upon reasonable request.

Received: 4 June 2020; Accepted: 23 October 2020;

Published online: 13 November 2020

REFERENCES

- Wang, H. & Kim, D. H. Perovskite-based photodetectors: materials and devices. *Chem. Soc. Rev.* **46**, 5204–5236 (2017).
- Sekitani, T. et al. Stretchable active-matrix organic light-emitting diode display using printable elastic conductors. *Nat. Mater.* **8**, 494–499 (2009).
- Tian, W., Min, L., Cao, F. & Li, L. Nested inverse opal perovskite toward superior flexible and self-powered photodetection performance. *Adv. Mater.* **32**, 1906974 (2020).
- Hu, W. et al. High-performance flexible photodetectors based on high-quality perovskite thin films by a vapor-solution method. *Adv. Mater.* **29**, 1703256 (2017).
- Rim, Y. S., Bae, S. H., Chen, H., De Marco, N. & Yang, Y. Recent progress in materials and devices toward printable and flexible sensors. *Adv. Mater.* **28**, 4415–4440 (2016).
- Stranks, S. D. et al. Electron-hole diffusion lengths exceeding 1 micrometer in an organometal trihalide perovskite absorber. *Science* **342**, 341–344 (2013).
- Jeon, N. J. et al. Compositional engineering of perovskite materials for high-performance solar cells. *Nature* **517**, 476–480 (2015).
- Miyata, A. et al. Direct measurement of the exciton binding energy and effective masses for charge carriers in organic–inorganic tri-halide perovskites. *Nat. Phys.* **11**, 582–587 (2015).
- Park, N.-G. Perovskite solar cells: an emerging photovoltaic technology. *Mater. Today* **18**, 65–72 (2015).
- Xing, G. et al. Low-temperature solution-processed wavelength-tunable perovskites for lasing. *Nat. Mater.* **13**, 476 (2014).
- Saraf, R., Pu, L. & Maheshwari, V. A light harvesting, self-powered monolith tactile sensor based on electric field induced effects in MAPbI₃ perovskite. *Adv. Mater.* **30**, 1705778 (2018).
- Cao, F., Tian, W., Wang, M., Cao, H. & Li, L. Semitransparent, flexible, and self-powered photodetectors based on ferroelectricity-assisted perovskite nanowire arrays. *Adv. Funct. Mater.* **29**, 1901280 (2019).
- Asuo, I. M. et al. Highly efficient and ultrasensitive large-area flexible photodetector based on perovskite nanowires. *Small* **15**, 1804150 (2019).
- Zhou, Q. et al. Nanochannel-assisted perovskite nanowires: from growth mechanisms to photodetector applications. *ACS Nano* **12**, 8406–8414 (2018).
- Hu, X. et al. High-performance flexible broadband photodetector based on organolead halide perovskite. *Adv. Funct. Mater.* **24**, 7373–7380 (2014).
- Tong, G. et al. Dual-phase CsPbBr₃-CsPb₂Br₅ perovskite thin films via vapor deposition for high-performance rigid and flexible photodetectors. *Small* **14**, 1702523 (2018).
- Li, C. et al. Ultrafast and broadband photodetectors based on a perovskite/organic bulk heterojunction for large-dynamic-range imaging. *Light Sci. Appl.* **9**, 31 (2020).
- Li, S. X. et al. Perovskite single-crystal microwire-array photodetectors with performance stability beyond 1 year. *Adv. Mater.* **32**, 2001998 (2020).
- Chen, S. et al. A flexible UV–Vis–NIR photodetector based on a perovskite/conjugated-polymer composite. *Adv. Mater.* **28**, 5969–5974 (2016).
- Wang, M., Cao, F., Meng, L., Tian, W. & Li, L. High-performance flexible self-powered photodetector based on perovskite and low-temperature processed In₂S₃ nanoflake film. *Adv. Mater. Interfaces* **6**, 1801526 (2019).
- Wang, D. et al. Chemical formation of soft metal electrodes for flexible and wearable electronics. *Chem. Soc. Rev.* **47**, 4611–4641 (2018).
- Saraf, R. & Maheshwari, V. Pbl₂ initiated cross-linking and integration of a polymer matrix with perovskite films: 1000 h operational devices under ambient humidity and atmosphere and with direct solar illumination. *ACS Appl. Energy Mater.* **2**, 2214–2222 (2019).
- Saraf, R., Tsui, T. & Maheshwari, V. Modulation of mechanical properties and stable light energy harvesting by poling in polymer integrated perovskite films: a wide range, linear and highly sensitive tactile sensor. *J. Mater. Chem. A* **7**, 14192–14198 (2019).
- Li, D. et al. Plasmonic photonic crystals induced two-order fluorescence enhancement of blue perovskite nanocrystals and its application for high-performance flexible ultraviolet photodetectors. *Adv. Funct. Mater.* **28**, 1804429 (2018).
- Zhou, J. & Huang, J. Photodetectors based on organic-inorganic hybrid lead halide perovskites. *Adv. Sci.* **5**, 1700256 (2018).
- Saraf, R. & Maheshwari, V. Self-powered photodetector based on electric-field-induced effects in MAPbI₃ perovskite with improved stability. *ACS Appl. Mater. Interfaces* **10**, 21066–21072 (2018).
- Lim, S., Ha, M., Lee, Y. & Ko, H. Large-area, solution-processed, hierarchical MAPbI₃ nanoribbon arrays for self-powered flexible photodetectors. *Adv. Opt. Mater.* **6**, 1800615 (2018).
- Zhang, T. et al. Low-temperature processed inorganic perovskites for flexible detectors with a broadband photoresponse. *Nanoscale* **11**, 2871–2877 (2019).
- Wu, W. et al. Flexible Photodetector arrays based on patterned CH₃NH₃PbI_{3-x}Cl_x perovskite film for real-time photosensing and imaging. *Adv. Mater.* **31**, 1805913 (2019).
- Song, J. et al. Monolayer and few-layer all-inorganic perovskites as a new family of two-dimensional semiconductors for printable optoelectronic devices. *Adv. Mater.* **28**, 4861–4869 (2016).
- Luo, X. et al. Ultrasensitive flexible broadband photodetectors achieving pA scale dark current. *npj Flex. Electron.* **1**, 1–8 (2017).
- Teng, C. et al. Organic dye-sensitized CH₃NH₃PbI₃ hybrid flexible photodetector with bulk heterojunction architectures. *ACS Appl. Mater. Interfaces* **8**, 31289–31294 (2016).
- Deng, W. et al. All-sprayed-processable, large-area, and flexible perovskite/MXene-based photodetector arrays for photocommunication. *Adv. Opt. Mater.* **7**, 1801521 (2019).
- Cao, F., Tian, W., Meng, L., Wang, M. & Li, L. Ultrahigh-performance flexible and self-powered photodetectors with ferroelectric P(VDF-TrFE)/perovskite bulk heterojunction. *Adv. Funct. Mater.* **29**, 1808415 (2019).
- Liu, H. et al. A high-performance photodetector based on an inorganic perovskite-ZnO heterostructure. *J. Mater. Chem. C* **5**, 6115–6122 (2017).
- Li, X. et al. Constructing fast carrier tracks into flexible perovskite photodetectors to greatly improve responsivity. *ACS Nano* **11**, 2015–2023 (2017).
- Xia, H. et al. Flexible and air-stable perovskite network photodetectors based on CH₃NH₃PbI₃/C8BTBT bulk heterojunction. *Appl. Phys. Lett.* **112**, 233301 (2018).
- Wang, Y. et al. Compositional engineering of mixed-cation lead mixed-halide perovskites for high-performance photodetectors. *ACS Appl. Mater. Interfaces* **11**, 28005–28012 (2019).
- Saraf, R., Mathur, A. & Maheshwari, V. Polymer-controlled growth and wrapping of perovskite single crystals leading to better device stability and performance. *ACS Appl. Mater. Interfaces* **12**, 25011–25019 (2020).
- Li, J., Dong, Q., Li, N. & Wang, L. Direct evidence of ion diffusion for the silver-electrode-induced thermal degradation of inverted perovskite solar cells. *Adv. Energy Mater.* **7**, 1602922 (2017).
- Behrouznejad, F., Shahbazi, S., Taghavinia, N., Wu, H. P. & Diau, E. W. G. A study on utilizing different metals as the back contact of CH₃NH₃PbI₃ perovskite solar cells. *J. Mater. Chem. A* **4**, 13488–13498 (2016).
- Boyd, C. C. et al. Barrier design to prevent metal-induced degradation and improve thermal stability in perovskite solar cells. *ACS Energy Lett.* **3**, 1772–1778 (2018).
- Shi, Y. et al. Synthesis and applications of silver nanowires for transparent conductive films. *Micromachines* **10**, 330 (2019).
- Lee, E. J., Chang, M. H., Kim, Y. S. & Kim, J. Y. High-pressure polyol synthesis of ultrathin silver nanowires: electrical and optical properties. *APL Mater.* **1**, 042118 (2013).

ACKNOWLEDGEMENTS

This work was supported by the Mitacs through the Mitacs Globalink Research Award program, University of Waterloo, Canada Foundation for Innovation, Early researcher award from Ministry of research and innovation and science, Ontario and NSERC Canada.

AUTHOR CONTRIBUTIONS

R.S. and H.F. contributed equally to this work. V.M. and R.S. planned the idea, R.S. and H.F. conducted the experiments, and all authors analyzed and discussed the results and contributed to the writing of the manuscript.

COMPETING INTERESTS

The authors declare no competing interests.

ADDITIONAL INFORMATION

Supplementary information is available for this paper at <https://doi.org/10.1038/s41528-020-00094-5>.

Correspondence and requests for materials should be addressed to V.M.

Reprints and permission information is available at <http://www.nature.com/reprints>

Publisher's note Springer Nature remains neutral with regard to jurisdictional claims in published maps and institutional affiliations.



Open Access This article is licensed under a Creative Commons Attribution 4.0 International License, which permits use, sharing, adaptation, distribution and reproduction in any medium or format, as long as you give appropriate credit to the original author(s) and the source, provide a link to the Creative Commons license, and indicate if changes were made. The images or other third party material in this article are included in the article's Creative Commons license, unless indicated otherwise in a credit line to the material. If material is not included in the article's Creative Commons license and your intended use is not permitted by statutory regulation or exceeds the permitted use, you will need to obtain permission directly from the copyright holder. To view a copy of this license, visit <http://creativecommons.org/licenses/by/4.0/>.

© The Author(s) 2020